TU Delft

Delft University of Technology

Disentangling Currents and Waves

Exploitation of Polarization Diversity for Wave-Doppler Estimation

O'Driscoll, Owen; Lopez-Dekker, Paco; Chapron, Bertrand

DOI
10.1109/TGRS.2025.3621914

Publication date
2025

Document Version
Final published version

Published in
IEEE Transactions on Geoscience and Remote Sensing

Citation (APA)
O'Driscoll, O., Lopez-Dekker, P., & Chapron, B. (2025). Disentangling Currents and Waves: Exploitation of Polarization Diversity for Wave-Doppler Estimation. *IEEE Transactions on Geoscience and Remote Sensing*, *63*, Article 4213512. https://doi.org/10.1109/TGRS.2025.3621914

Important note
To cite this publication, please use the final published version (if applicable).
Please check the document version above.

Copyright
Other than for strictly personal use, it is not permitted to download, forward or distribute the text or part of it, without the consent of the author(s) and/or copyright holder(s), unless the work is under an open content license such as Creative Commons.

Takedown policy
Please contact us and provide details if you believe this document breaches copyrights.
We will remove access to the work immediately and investigate your claim.

This work is downloaded from Delft University of Technology.
For technical reasons the number of authors shown on this cover page is limited to a maximum of 10.

Green Open Access added to TU Delft Institutional Repository
as part of the Taverne amendment.

More information about this copyright law amendment
can be found at https://www.openaccess.nl.

Otherwise as indicated in the copyright section:
the publisher is the copyright holder of this work and the
author uses the Dutch legislation to make this work public.

Disentangling Currents and Waves: Exploitation of Polarization Diversity for Wave-Doppler Estimation

Owen O'Driscoll, Paco López-Dekker, *Senior Member, IEEE*, and Bertrand Chapron

***Abstract*—Surface velocities measured by synthetic aperture radar (SAR) contain contributions from both mean surface motion—referred to as total surface current (TSC)—and the often more prominent sea-state-induced wave motions. Most modern SAR systems cannot distinguish between these two phenomena, which has stifled TSC retrieval from SAR data for decades. We propose a new framework to separate TSC and wave-motion components by leveraging polarization diversity, exploiting the tendency of each phenomenon to imprint distinct signatures on orthogonal polarizations. Building on a foundational signal model, we derive four source-separation algorithms. To address the model's theoretical limitations, we introduce empirical extensions via symbolic regression, guided by varying levels of theoretical insight. The developed algorithms are evaluated using simulated C-band SAR data and benchmarked against a reference geophysical model function (GMF) implementation. Our methods demonstrate comparable overall performance, with errors on the order of $\mathcal{O}$(0.1 m/s), and notably outperform the GMF in resolving kilometer-scale spatial features—a domain where traditional GMFs generally struggle. Preliminary results obtained on TanDEM-X observations confirm the generalizability of our approach. These findings highlight the potential of future SAR missions with polarimetric capabilities, such as Harmony, to achieve high-resolution separation of surface-motion sources using polarization diversity.**

***Index Terms*—Polarization diversity, surface currents, surface motion, synthetic aperture radar (SAR), wave Doppler.**

I. Introduction

THE potential of synthetic aperture radar (SAR) to retrieve surface Doppler—and thus surface velocity—has been investigated by many authors [1], [2], [3], [4], [5], [6]. The observed surface velocity should be understood as an average of the line-of-sight (LoS) projection of the instantaneous velocities of each *scatterer* on the surface, weighted by their radar cross sections. Ocean waves modulate the local normalized radar cross section (NRCS). The main contributors to this modulation—tilt and hydrodynamic modulation—affect different parts of the wave to different degrees [7], [8]. The ensuing correlation between the modulated NRCS and orbital velocities results in an effective Doppler velocity, often referred to as the wave Doppler, even in the absence of any mean surface motion [9]. Indeed, it is well established that the Doppler can be used to infer the surface wind. In general, the measured Doppler velocity due to wind-driven waves is in the order of 10%–20% of the surface wind [7].

Aside from this wave Doppler, the measured Doppler velocity also includes the LoS projection of the actual mean surface motion, often referred to as the total surface current (TSC).

Naturally, one would need to distinguish between the wave Doppler and the current Doppler when interested only in the latter. Considering that the wave Doppler may easily exceed the TSC Doppler, an accurate separation is paramount.

The wave Doppler also has intrinsic value beyond its use in targeting a TSC; it captures information on the wave state which relates to a host of air–sea coupling processes (see [10], [11], [12]) and, due to its close correlation to surface winds, it can also be used in improved surface–wind estimation [13], [14], [15].

Contemporary wave-Doppler estimation techniques use empirical geophysical model functions (GMFs). These models, such as CDOP, XDOP, and KaDOP [13], [16], [17], are tuned to provide a good average fit as a function of wind speed. Theory (see [8], [18]) tells us that the wave Doppler depends on the wave spectra and wave-breaking fraction and that these depend on many factors, including wave–current and wave–wave interactions. Neglecting departures from the mean state for these factors may inadvertently lead to models capable of estimating wave Doppler only when no surface-current gradients are present—an undesirable trait.

More holistic models (see [19], [20]) consider additional information relating to the wave state, making them more suitable to disentangle the convoluted Doppler signals. Still, these models implicitly rely on the nonexistence of wind–wave–current interactions or require ancillary data such as directional wind, wave, and swell information.

In this work, we rely on an untapped resource for the estimation of the wave Doppler: polarization diversity. It is known that the measured Doppler velocity is polarization-dependent, which should be generally attributed to a polarization dependence of the wave Doppler. This dependence has previously been exploited to estimate the surface wind [14].

The potential to exploit polarization diversity in this sense was already anticipated in the literature [7], [21] and was incorporated in the original SEASTAR system concept [22], which was conceived as a hybrid polarimetric system [23]. The Harmony mission [24] also features a bistatic equivalent to a hybrid polarized system.

Received 11 July 2025; revised 7 October 2025; accepted 11 October 2025. Date of publication 15 October 2025; date of current version 19 November 2025. This work was supported by the European Space Agency (ESA) under Contract RFP/3-18663/24/NL/IB/ar. *(Corresponding author: Owen O'Driscoll.)*

Owen O'Driscoll and Paco López-Dekker are with the Department of Geoscience and Remote Sensing, Delft University of Technology, 2628 CN Delft, The Netherlands (e-mail: o.p.odriscoll@tudelft.nl).

Bertrand Chapron is with Laboratoire d'Océanographie Physique et Spatiale IFREMER, 29280 Plouzané, France

Digital Object Identifier 10.1109/TGRS.2025.3621914

1558-0644 © 2025 IEEE. All rights reserved, including rights for text and data mining, and training of artificial intelligence and similar technologies. Personal use is permitted, but republication/redistribution requires IEEE permission.
See https://www.ieee.org/publications/rights/index.html for more information.

Authorized licensed use limited to: TU Delft Library. Downloaded on December 03,2025 at 16:28:38 UTC from IEEE Xplore. Restrictions apply.

From a signal model based on the Doppler-shift considering radar imaging model DopRIM, [8], [18], we derive a closed-form expression for the wave Doppler as a function of polarized observables. We assume that the Doppler originating from the TSC is polarization-independent. Therefore, the polarized Doppler difference removes the TSC component, providing direct insights into the wave-Doppler contributions. Through careful weighting of this difference, we obtain a quantitative estimate of the wave Doppler. We further introduce a simplified approximation tailored to practical use.

The scarce nature of clear validation data hinders the assessment of the estimated wave- and TSC-Dopplers; measurements of two-dimensional surface currents are lacking, and no existing dataset dissects the sources of the NRCS and Doppler at relevant scales. To overcome this obstacle, we rely on simulated data by employing Harmony's scientific workbench (SWB) to simulate relevant contributions toward the total NRCS and Doppler budgets. This simulator combines state-of-the-art radar scattering models with ancillary data from a coupled air–sea model. Afterward, the developed methodology is applied to a limited quantity of observational data obtained with TanDEM-X [25].

Our signal model is presented in Section II, from which idealized separation of scattering sources can be deduced. The signal model will be applied to simulations and observations, and these are detailed in Section III, with the results of this application, and a discussion thereof, presented in Section IV. Conclusions and perspectives are shared in Section V.

II. Signal Model

We follow [26], [27] assuming that the NRCS for a co-polarization PP (in this article HH or VV) can be written as the sum of a polarized scattering term σ_r^{PP}, well described by rough surface scattering theory, and a nonpolarized scalar term, σ_s, assumed to be caused by specular scattering associated with localized steep slopes caused by breaking waves

$$\sigma_0^{\mathrm{PP}} = \sigma_r^{\mathrm{PP}} + \sigma_s. \tag{1}$$

The first term has often been associated with *Bragg* scattering in a two-scale model. Given the difficulties associated with such a model, with a somewhat arbitrary division of scales, we opt to follow the symbol convention used in [18], referring to the regular surface, instead of referring to it as σ_B^{PP}. Note that (1) implicitly assumes that the complex-valued contributions of the two types of scatterers are uncorrelated.

As in [26], we define the polarization ratio, which can be estimated from the data

$$p = \frac{\sigma_0^{\mathrm{HH}}}{\sigma_0^{\mathrm{VV}}}. \tag{2}$$

For convenience, we can also define the fraction of scalar (wave-breaking) scattering for any polarization, for example,

$$f_s^{\mathrm{HH}} = \frac{\sigma_s}{\sigma_0^{\mathrm{HH}}} \tag{3}$$

or, at vertical polarization

$$f_s^{\mathrm{VV}} = p f_s^{\mathrm{HH}}. \tag{4}$$

We now extend this decomposition to the geophysical Doppler velocity, v^{PP}. This Doppler velocity can be derived from an along-track interferometry (ATI) phase, or from a Doppler centroid anomaly (DCA). We will assume that the Doppler velocity can be written as

$$v^{\mathrm{PP}} = v_{\mathrm{wD}}^{\mathrm{PP}} + v_{\mathrm{TSC}} \tag{5}$$

the sum of a so-called wave-Doppler component and a term associated with the TSC. Conceptually, this decomposition assumes that the waves propagate relative to a medium that moves with a velocity given by the TSC vector. One could reasonably assume that wave–current interactions affect different waves differently, and, in turn, different waves affect both polarizations differently. We assume this effect is minimal, such that v_{TSC} can be considered polarization-independent. Furthermore, possible complications associated with a nonconstant vertical current profile are ignored, and we assume that the Doppler velocities can be traced uniquely to either source.

The wave-Doppler velocity component can be written as the weighted average of the Doppler velocities associated with the regular surface, v_r, and to wave breaking, v_s, where the weighting is given by the scattering fractions

$$v_{\mathrm{wD}}^{\mathrm{PP}} = v_r^{\mathrm{PP}} \cdot \left(1 - f_s^{\mathrm{PP}}\right) + v_s \cdot f_s^{\mathrm{PP}}. \tag{6}$$

Considering two co-polarized measurements only, (5) and (6) involve four unknown velocity contributions with two velocity observables.

Since the surface current is polarization-independent, its contribution is removed by studying the velocity difference, which, when written in terms of the predefined variables, yields

$$\begin{aligned} v^{\mathrm{HH}} - v^{\mathrm{VV}} = \; & v_r^{\mathrm{HH}}\left(1 - f_s^{\mathrm{HH}}\right) - v_r^{\mathrm{VV}}\left(1 - f_s^{\mathrm{VV}}\right) \\ & + v_s\left(f_s^{\mathrm{HH}} - f_s^{\mathrm{VV}}\right). \end{aligned} \tag{7}$$

In general, all components will depend on the observation geometry and sea state. We can, however, always define the ratios of the wave Dopplers with respect to one of them. This way, we introduce

$$k_r = \frac{v_r^{\mathrm{HH}}}{v_r^{\mathrm{VV}}} \tag{8}$$

and

$$k_s = \frac{v_s}{v_r^{\mathrm{VV}}}. \tag{9}$$

These ratios are generally positive, though changing wind directions may yield local negative values.

Now the resonant scattering can be isolated. When written in terms containing only HH polarization, by combining (7) with (4), (8) and (9), this yields

$$v_r^{\mathrm{HH}} = \frac{\left(v^{\mathrm{HH}} - v^{\mathrm{VV}}\right)}{1 - f_s^{\mathrm{HH}} - \frac{1}{k_r}\left(1 - p f_s^{\mathrm{HH}}\right) + \frac{k_s}{k_r} f_s^{\mathrm{HH}}\left(1 - p\right)}. \tag{10}$$

We next rearrange (10) and combine it with (6) to yield a closed-form expression for the wave Doppler

$$\begin{aligned} v_{\mathrm{wD}}^{\mathrm{HH}} &= v_r^{\mathrm{HH}}\left(1 - f_s^{\mathrm{HH}}\right) + v_s f_s^{\mathrm{HH}} \\ &= v_r^{\mathrm{HH}}\left(1 - f_s^{\mathrm{HH}} + \frac{k_s}{k_r} f_s^{\mathrm{HH}}\right) \end{aligned}$$

Authorized licensed use limited to: TU Delft Library. Downloaded on December 03,2025 at 16:28:38 UTC from IEEE Xplore. Restrictions apply.

$$= \left(1 - f_s^{\mathrm{HH}} + \frac{k_s}{k_r} f_s^{\mathrm{HH}}\right) \cdot \frac{\left(v^{\mathrm{HH}} - v^{\mathrm{VV}}\right)}{1 - f_s^{\mathrm{HH}} - \frac{1}{k_r}\left(1 - p f_s^{\mathrm{HH}}\right) + \frac{k_s}{k_r} f_s^{\mathrm{HH}}(1-p)}. \quad (11)$$

The obtained formulation is a weighted polarized Doppler difference, which, following (5), should be free from contamination by the TSC Doppler. In this rather cumbersome form, k_r, k_s, and f_s^{HH} are still unknown. Their variability will be investigated in Section III-A4.

The same derivation can easily be made using v_r^{VV} instead of v_r^{HH} by combining (10), (8), and (6), yielding

$$v_{\mathrm{wD}}^{\mathrm{VV}} = \left(1 - f_s^{\mathrm{VV}} + k_s f_s^{\mathrm{VV}}\right) \cdot \frac{\left(v^{\mathrm{HH}} - v^{\mathrm{VV}}\right)}{k_r\left(1 - \frac{f_s^{\mathrm{VV}}}{p}\right) - 1 + f_s^{\mathrm{VV}}\left(k_s \frac{1-p}{p} + 1\right)}. \quad (12)$$

Though practically the same as (11), this formulation is less convenient to simplify, as will be shown later in (25).

III. Data Overview

Lacking ground-truth measurements, we instead rely on simulations obtained with Harmony's SWB. Details on the simulator are provided in Section III-A.

Next, we apply the developed framework to a limited dataset of dual-polarized ATI observations made with TanDEM-X. This observational data is described in Section III-B. Additional processing details are provided in Appendix A.

A. Simulation Data

1) Scientific Work Bench: The SWB employs state-of-the-art versions of the radar imaging model (RIM) [18], [28] and Doppler RIM (DopRIM) [7], [8], [29], [30] to simulate polarimetric NRCS and Doppler for bi-and monostatic spaceborne observations of the ocean surface. SWB inputs include surface currents, sea surface temperatures (SST), wind/stress, and interior currents. For the simulations used in this article, we use SWAN Simulating WAves-Nearshore, [31] to generate the long-wave directional spectra, with the limit between what we consider long and short waves set at ten times the wavenumber of the spectral peak, $10k_p$. Subsequently, the RIM model generates the short-wave spectra and the breaking wave fraction, considering the long-wave spectrum, the local wind, and modulations due to surface current gradients.

The forward model simulates observations based on the Sentinel-1 interferometric wide-swath (IW) mode. Specular reflection can be ignored at this range of incidence angles (see Fig. 2 in [18]), and the NRCS is fully attributed to resonant regular scattering and wave breaking, as in (1), with the wave-breaking fraction, hydrodynamic modulation, and wave tilting all taken into account.

We emulate a hypothetical dual co-polarized ATI mode for Sentinel-1. Representative noise at the burst level is added to the NRCS. A 2-Hz Gaussian uncertainty is added to the simulated Doppler, in line with a pessimistic ATI performance (see [4]). Model outputs are provided at a 1 by 1 km grid spacing.

2) DopRIM-GMF: In addition to the forward model, the SWB uses DopRIM to provide a look-up table (LUT) for the expected Doppler and NRCS given a wind magnitude/direction, incidence angle, polarization, and wave age—much like conventional GMFs such as CDOP and CMOD. The estimated wave Dopplers will be compared to those predicted by this purpose-built LUT, referred to as the DopRIM-GMF.

The DopRIM-GMF and the SWB forward model are closely related: the DopRIM-GMF is generated from the SWB forward model using an Elfouhaily long-wave spectrum [32]—as opposed to the SWAN-derived long-wave spectrum for the reference SWB runs—zero currents, a homogeneous wind, and a constant inverse wave age. The latter we approximate by 1.2, which corresponds to a developing sea.

Since both the DopRIM-GMF and the SWB forward model use DopRIM, we expect no biases between these models (except local biases that may result from disparate parameterization of wave–wave and wave–current interactions). This enables a fairer illustration of GMF performance, as, in practice, biases can be fixed by tuning.

Furthermore, in all uses of the DopRIM-GMF, the "true" model winds are used, representing a highly idealized GMF performance.

3) Case Study: The SWB simulation covers a region off the Californian coast where a spatially varying system of currents and winds causes a dynamic range of local conditions. An overview of the coupled input parameters to the SWB and SWAN is presented in Fig. 1.

The upper right-hand side of the domain contains regions with colder sea surface temperatures associated with the Californian coastal upwelling. The resulting swirling system of surface currents locally exceeds 1 m/s. In addition to the surface currents, distinct wind regimes reign supreme: winds accelerate toward the coast, nearing 20 m/s toward the East, and a shift in wind direction toward the South coincides with several streak-like figures. The dynamic wind speed range exceeds 10 m/s.

4) Variability of Unknowns: Using the SWB, we obtain a closed budget for the NRCS and Doppler contributions. Namely, how much regular scattering and wave breaking contribute to the would-be-observed NRCS and Doppler. It should be noted that the Doppler originating from wind–wave–current interactions is fully ascribed to the wave Doppler, even though its conception necessitates the presence of surface-current gradients. The Doppler budget contains an additional signal originating from the total LoS-projected surface current.

Working with modeled data gives us access to the terms k_r, k_s, and f_s^{HH}, as defined in Section II. Distributions of these spatially varying quantities are presented in Fig. 2. The calculation of the therein presented $\tilde{k}_s$ will be discussed later. The targeted wave Dopplers converted to a surface-projected velocity vary from approximately 0 m/s in cross-wind conditions to 1–2 m/s over the remainder of the domain.

B. Observational Data

In addition to simulations, we apply our signal model on a unique dataset of dual-polarized ATI observations obtained with TanDEM-X [25] in a formation configuration optimized

Authorized licensed use limited to: TU Delft Library. Downloaded on December 03,2025 at 16:28:38 UTC from IEEE Xplore. Restrictions apply.

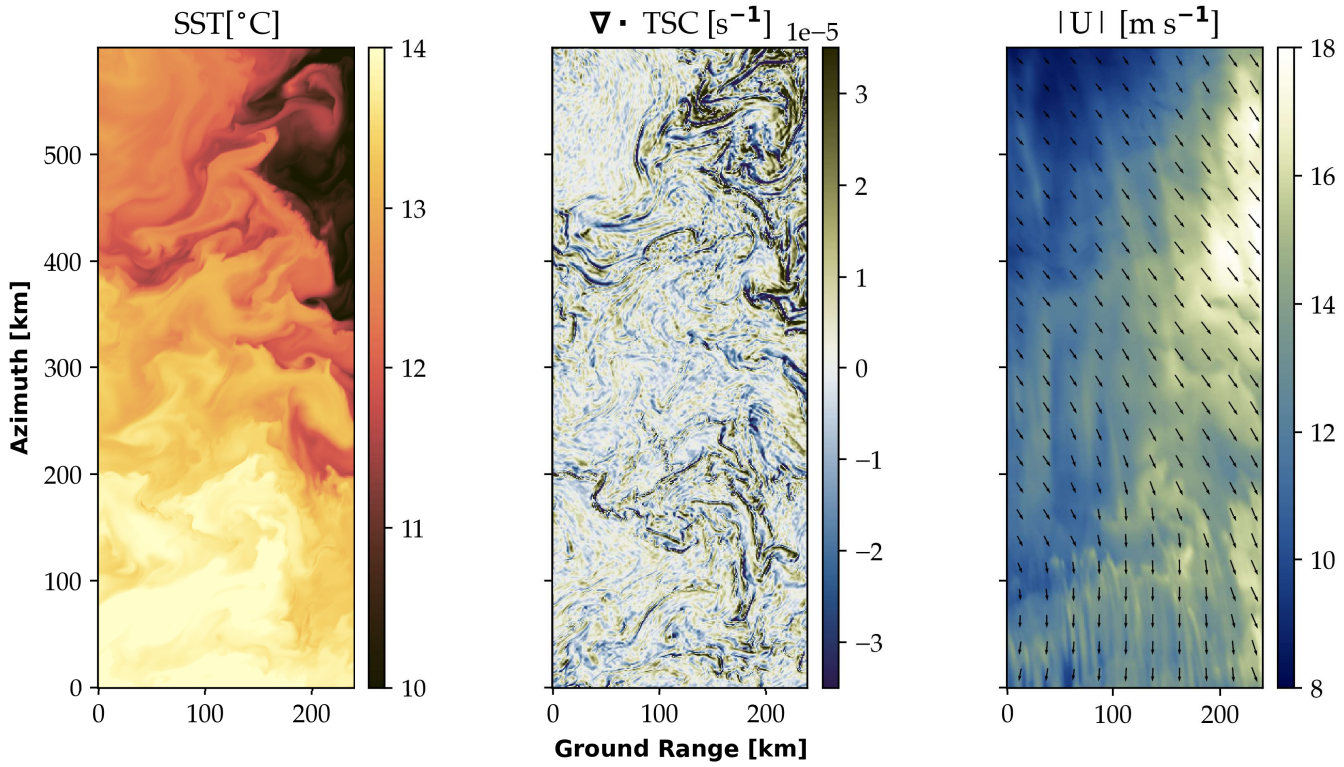

Fig. 1. Overview of model inputs for the Californian case study overlapping with the forward model output. Coordinates follow those of the simulated right-looking observations system. True North is oriented approximately 15° clockwise from azimuth. (Left) Sea surface temperatures, (center) divergence of the TSC, (right) wind-field magnitude at 10 m with corresponding directions.

for along-track interferometry. No in situ validation is available for these observations, enabling a qualitative analysis only.

The TanDEM-X data was acquired in descending passes between 2014-08-30 and 2014-09-15 at around 06:00 UTC, over the coastal region East of Cap de Creus, on the Catalan sea. The system was operated in a dual co-polarized stripmap mode, interleaving horizontally and vertically polarized transmit pulses to provide simultaneous interferometric pairs of HH and VV images. Results are presented for the scenes acquired with a 41° incident angle, for which strong polarimetric signatures are expected.

IV. Results and Discussion

Results are separated into three categories: first, introducing the developed retrieval algorithms in Section IV-A, followed by the results of these algorithms applied on SWB data in Section IV-B. The analyses made using the SWB aim to assess the validity of our signal model, the variability of presumed constants, and the suitability of proposed approximations. Next, we apply the approximation learned from model data to real data. Since no quantitative validation data exists for the TanDEM-X case study, a qualitative assessment is performed instead in Section IV-C.

A. Retrieval Algorithm Design

The analytical forms in (11) and (12) contain too many unknowns for them to be applied without a priori knowledge. As a workaround, we establish various simplified versions that require no a priori information and could thus be applied to any dual-polarized data. The first such method will discard the variability of k_r, k_s, and f_s^{HH} and approximate them by a constant. The second and third methods aim to predict the previously discarded variability by means of symbolic regression with the radar observables, thus forming a hybrid model that relies on empiricism as well as analytical formulations. The fourth and final method relies on an additional assumption which reduces the number of unknowns in (11) from three to one. The last remaining unknown can then be approximated by a constant, like in the first method, or by a proxy GMF, like in the second and third methods. This fortuitous cancellation of unknowns does not transfer to $v_{\mathrm{wD}}^{\mathrm{VV}}$ from (12), such that it can only be provided for $v_{\mathrm{wD}}^{\mathrm{HH}}$ from (11).

All empirical values needed for these four simplified versions are obtained from the upper-half of the California domain, which serves as the training data. This area covers the full range of incident angles and includes a region with wind–wave–current interactions. The lower-half, on which empirical methods are assessed, also contains currents as well as a transient wind regime. The latter is unsampled in the upper-half and thus provides insights into the transferability of empirical methods. Then, we resimulate a new realization of the California scene under a different viewing geometry—a descending instead of ascending orbit—for an overlapping section of the original scene. This resimulated scene covers most of the original test area, along with a sliver of the training

Authorized licensed use limited to: TU Delft Library. Downloaded on December 03,2025 at 16:28:38 UTC from IEEE Xplore. Restrictions apply.

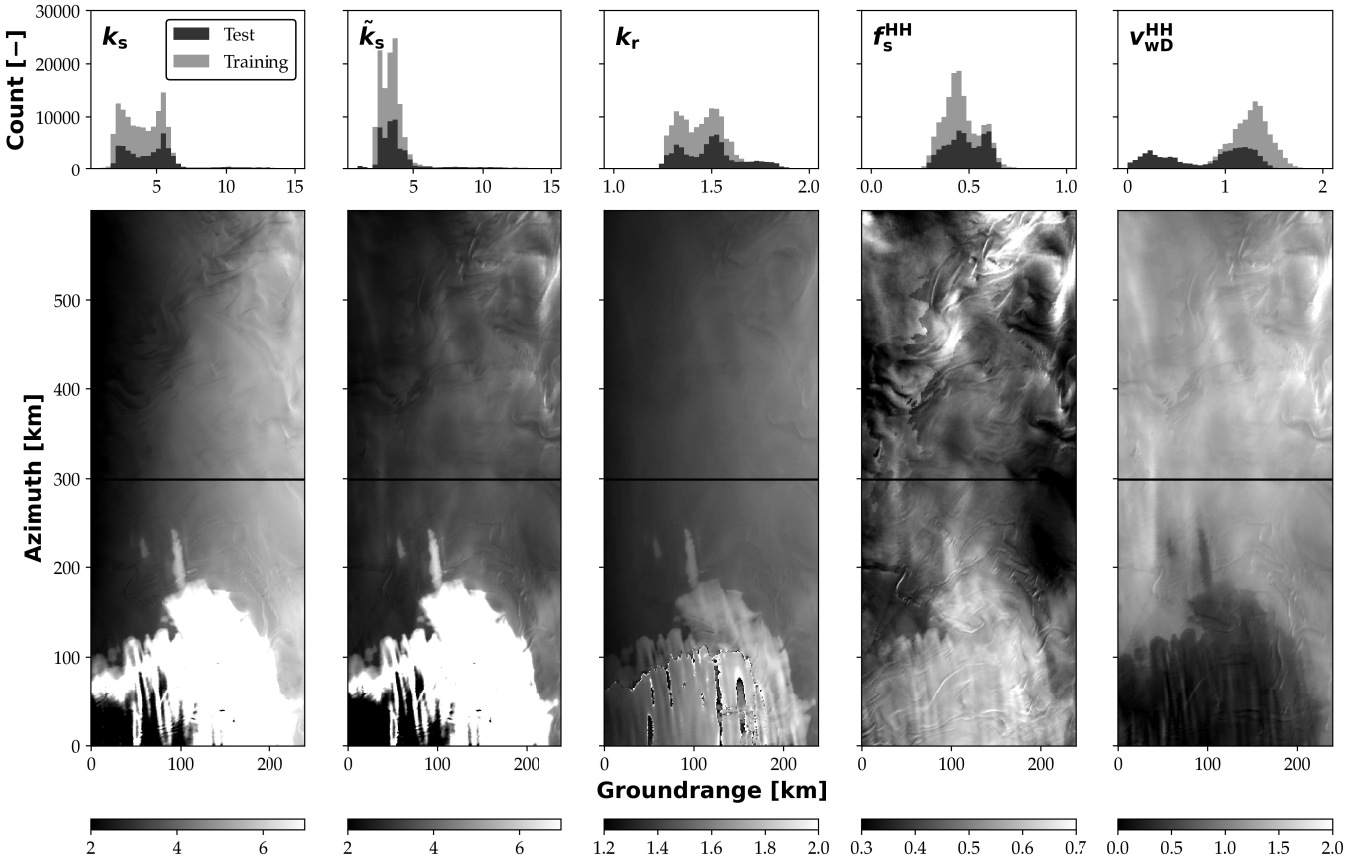

Fig. 2. Absolute values of: (upper) distribution of unknowns in (11) and (25) as simulated under noise-free conditions; (lower) corresponding spatial distribution. The black horizontal line separates the North/South training/test data, respectively. Exploding values of k_s and $\tilde{k}_s$ in the southern half are caused by a cross-wind, resulting in the Doppler magnitude approaching zero.

area, and it enables us to assess the generalizability of models trained and calibrated under different observation conditions. Development details for the individual models are given below.

1) Constants: We ignore the variability in k_r, k_s, and f_s^{HH} and ascribe to them a constant value. These constants are obtained by selecting the median value over the training subset of the simulation, as shown in Fig. 2.

2) Hybrid-A: Much of the variability in k_s and k_r is incident-angle-dependent, as follows from their formulations and Fig. 2. Similarly, following the formulations of f_s^{PP}, these are related to a ratio of scattering components. Thus, we next construct a hybrid model using the original analytical model supplemented by empirical components to predict known sources of parameter variance.

To that end, we employ symbolic regression in combination with the radar observables, yielding various functional approximations of the unknowns in question. Constructing robust empirical relations on a single case study is unfeasible. We discard suggested functional formulations that appear to make no physical sense, instead selecting those that balance simplicity (and therefore, hopefully, transferability) as well as accuracy. The selected functional forms are

$$k_s \approx e^{c_1 \cdot \theta_i} \tag{13}$$

$$k_r \approx c_2 \cdot e^{\theta_i} \tag{14}$$

$$f_s^{\mathrm{HH}} \approx \sin\left(p_{\mathrm{dB}}^{-1} - c_3\right) \tag{15}$$

$$f_s^{\mathrm{VV}} \approx \cos\left(c_4 \cdot p_{\mathrm{dB}}\right) \tag{16}$$

with the respective coefficients presented in Table I. The exact functional forms for k_s and k_r are not particularly important, more so that they can be considered constant at a given incidence angle. The formulations for f_s^{HH} and f_s^{VV} are more specific: the (co)sines prevent nonphysical values greater than one, while the (co)sine content represent a rescaled ratio of backscatter (with backscatter in dB), much like the formulation in (3).

3) Hybrid-B: Alternatively, and building on [26], we can substitute the empirical expressions for f_s^{PP} with one infused with theoretical understanding. First, the scalar scattering is formulated as a function of radar observables

$$\sigma_s = \sigma_0^{\mathrm{VV}} - \frac{\left(\sigma_0^{\mathrm{VV}} - \sigma_0^{\mathrm{HH}}\right)}{1 - p_r} \tag{17}$$

where the ratio of resonant scattering is indicated by

$$p_r = \frac{\sigma_r^{\mathrm{HH}}}{\sigma_r^{\mathrm{VV}}}. \tag{18}$$

A Taylor expansion for p_r is given in [26] as

$$p_r \approx \frac{|G_H|^2}{|G_V|^2}\left[1 + (g_H - g_V) \cdot \overline{s^2}\right] \tag{19}$$

Authorized licensed use limited to: TU Delft Library. Downloaded on December 03,2025 at 16:28:38 UTC from IEEE Xplore. Restrictions apply.

TABLE I
ANECDOTAL C-BAND COEFFICIENTS FOR APPROXIMATIONS CORRESPONDING TO THE CONSIDERED SIMPLIFICATION METHODS

1) Constants		2) Hybrid-A		3) Hybrid-B		4) simplified	
k_{s}	3.76	c_1	2.04	c_1	2.04	$\tilde{k}_{\mathrm{s}}$	3.32
k_{r}	1.42	c_2	0.73	c_2	0.73	k_{r}	-
$f_{\mathrm{s}}^{\mathrm{HH}}$	0.43	c_3	-0.35	c_5	1.69	$f_{\mathrm{s}}^{\mathrm{HH}}$	1
$f_{\mathrm{s}}^{\mathrm{VV}}$	0.23	c_4	1.09	c_6	$1.54{\cdot}10^{-2}$	$f_{\mathrm{s}}^{\mathrm{VV}}$	-

where $\overline{s^2}$ refers to the mean-squared slope and g_P to the second-order derivatives of $|G_P|$, which, in turn, are defined as

$$G_V = G_V\left(\theta - \zeta\left(\overline{s^2}\right)\right) \tag{20}$$

$$G_H = G_H\left(\theta - \zeta\left(\overline{s^2}\right)\right) + \left(\frac{\zeta\left(\overline{s^2}\right)}{\sin\theta}\right)^2 G_V(\theta) \tag{21}$$

with ζ indicating the tilting of presumed isotropic Gaussian slopes for waves with wavelengths several times greater than that of the resonant wavelengths [28].

To make use of this method, a priori estimates of $\overline{s^2}$ and wave spectra (for weighting) are needed. But these quantities are nontrivial to obtain in practice. Therefore, we create a surrogate expression that initially ignores the impact of $\overline{s^2}$ by replacing the original tilt considering $G_P(\zeta, \theta)$ with $G_P(\theta)$. Then, a compensation is added to account for the previously discarded $\overline{s^2}$. This compensation is again determined by symbolic regression, with the resulting formulations being

$$p_r \approx \frac{|G_H(\theta)|^2}{|G_V(\theta)|^2}\left[c_5 + c_6 \cdot \mathrm{dB}\left(\sigma_0^{\mathrm{VV}}\right)\right]. \tag{22}$$

Essentially, this formulation substitutes $\overline{s^2}$ with an alternative compensation dependent on the NRCS—a known $\overline{s^2}$ proxy. The magnitude of σ_0^{VV} at a given incidence angle is influenced by a multitude of other factors (primarily the relative wind direction with respect to the sensor), which may unfavorably affect p_r estimation. Combining (22) with (17) results in

$$f_s^{\mathrm{HH}} = \frac{\sigma_0^{\mathrm{VV}}}{\sigma_0^{\mathrm{HH}}} - \frac{\left(\sigma_0^{\mathrm{VV}} - \sigma_0^{\mathrm{HH}}\right)}{\sigma_0^{\mathrm{HH}}(1 - p_r)} \tag{23}$$

$$f_s^{\mathrm{VV}} = 1 - \frac{\left(\sigma_0^{\mathrm{VV}} - \sigma_0^{\mathrm{HH}}\right)}{\sigma_0^{\mathrm{VV}}(1 - p_r)}. \tag{24}$$

4) Simplified: In the preceding approaches, we have attempted to account for three unknowns. This was done either by assuming their invariability or, conversely, by attempting to predict their variability. Here, we proceed with a third method, which aims to reduce the complexity by selecting fortuitous and canceling combinations of the unknowns in question. The resulting simplified approximation exclusively applies to the estimation of $v_{\mathrm{wD}}^{\mathrm{HH}}$, which should pose no limitation as any estimate of v_{TSC} in combination with (5) enables estimation of the $v_{\mathrm{wD}}^{\mathrm{VV}}$ as well.

If we assume that f_s^{HH} has a constant value of 1, which implies that $\sigma_s = \sigma_0^{\mathrm{HH}}$—an unlikely condition, and not observed in Fig. 2—we eliminate unknown k_r. This approximation takes the form

$$v_{\mathrm{wD}}^{\mathrm{HH}} = \frac{\tilde{k}_s}{\tilde{k}_s - 1}\frac{1}{1 - p}\left(v_D^{\mathrm{HH}} - v_D^{\mathrm{VV}}\right) \tag{25}$$

where we can still use the equality sign because k_s has been exchanged with $\tilde{k}_s$, the only remaining unknown. To account for errors introduced by the above assumption, the distribution of the new $\tilde{k}_s$ has necessarily changed with respect to the "real" k_s (see Fig. 2). This also obscures an intuitive physical interpretation of $\tilde{k}_s$. Yet, the spread in $\tilde{k}_s$ decreases under idealized no-noise conditions when compared to k_s, making it easier to estimate. Thus, not only does this approach decrease the number of unknown parameters (from k_r, k_s, and f_s^{HH} to only $\tilde{k}_s$), it simultaneously decreases the spread in the remaining target parameter ($\sigma_{\tilde{k}_s} < \sigma_{k_s}$). Such gross approximations also negate potential exploding uncertainties resulting from compounding interactions between erroneous estimates of k_r, k_s, f_s^{HH}, and f_s^{VV}.

The challenge then is finding a suitable value for $\tilde{k}_s$. Fortunately, this formulation is relatively insensitive to uncertainty; reasonable results are obtained even when fixing $\tilde{k}_s$ to the tail ends of the $\tilde{k}_s$ distribution in Fig. 2 (not shown). The value used here is again obtained from the median value over the training subset.

B. Quantitative Model Analyses

The four approaches are compared to the wave Dopplers predicted by the SWB. Baseline estimates are also provided by the DopRIM-GMF, whose performance, as illustrative of GMFs, is added for comparison with the presented polarimetric methods.

Distributions of errors for the different cases are presented in Fig. 3. Empirically derived constants are presented in Table I. The results are discussed individually in the subsequent sections. Model performance is calculated at 1-km grid spacing, with the displayed results representing the distribution of mean values selected on a coarse-grained 3 by 3-km grid.

1) Constants: The majority of errors resulting from the fixed-value approach are contained within ±25 cm/s. By design, no bias is present in the training area, and only a minor bias appears in the test data. More problematic is the increased standard deviation, which is particularly prevalent in the elongated tails of the residuals for the descending orbit. This indicates that the constants approach is poorly transferable.

A more encouraging picture is revealed in Fig. 4: the constants approach extracts most of the local geophysical gradient, though leaving an along-range trend behind. Thus, even though the variability in unknowns is ignored, the gross simplifications still yield distributions in line with an idealized GMF, while the spatial performance enables enhanced retrieval of local features.

2) Hybrid-A and -B: As shown in Fig. 3, the resulting hybrid models A and B yield a narrower distribution around zero for the training data (as expected), which transfers well to both the test and descending cases, even when compared to the idealized DopRIM-GMF results. Observed uncertainties

Authorized licensed use limited to: TU Delft Library. Downloaded on December 03,2025 at 16:28:38 UTC from IEEE Xplore. Restrictions apply.

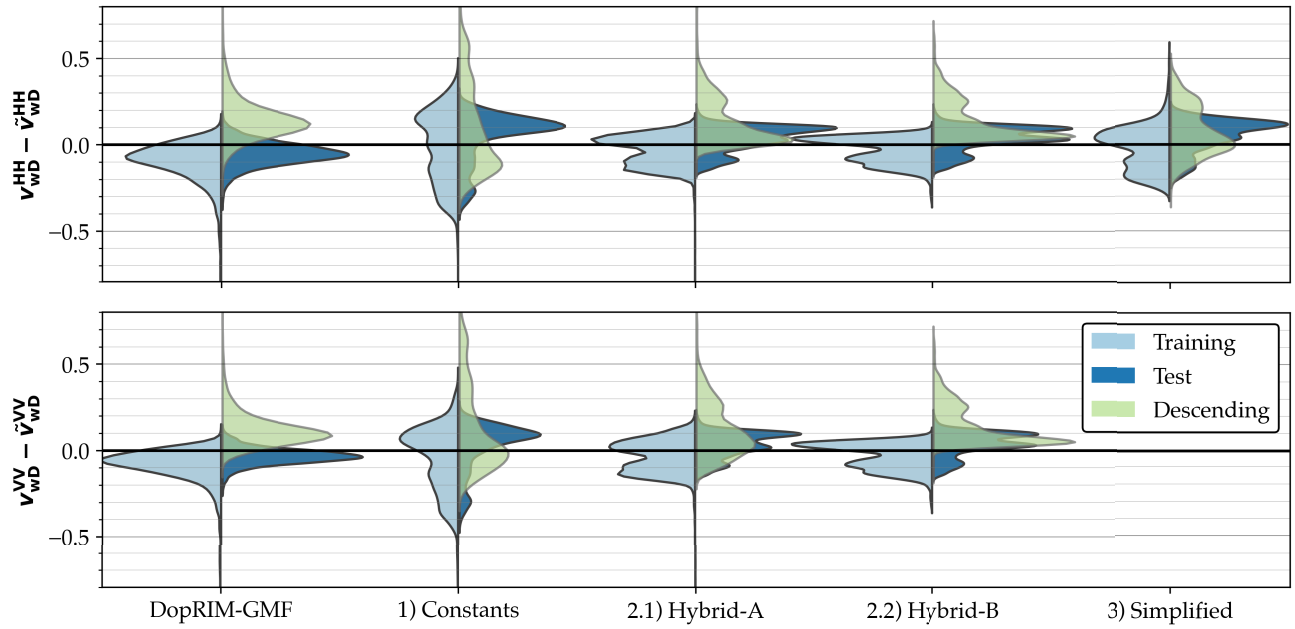

Fig. 3. Summary of analyses on the California case study using ascending (training + test) and descending simulations with no noise: (DopRIM-GMF) using idealized model winds in combination with the DopRIM-GMF, (constants) using the full analytical model but replacing the unknowns with constants, (hybrid-A and hybrid-B) using the full analytical model but replacing the unknowns with empirical relationships, (simplified) using the simplified analytical model and replacing the single unknown with a constant. Model performance is calculated at 1-km grid spacing, with the displayed results representing the distribution of mean values selected on a coarse-grained 3 by 3 km grid. The colored areas are weighted by relative occurrence. The total area of descending data differs from that of training and test, as the descending orbit does not fully overlap with the original domains. In the presence of noise, as defined in Section III-A, the standard deviation of residuals over the test area for the various scenarios increases from (left to right) 0.07, 0.14, 0.07, 0.07, and 0.09 m/s to 0.07, 0.20, 0.16, 0.16, and 0.18 m/s for HH and 0.05, 0.14, 0.07, and 0.07 m/s to 0.05, 0.17, 0.13, and 0.13 m/s for VV.

at $\mathcal{O}(0.1$ m/s) are an order of magnitude lower than the $\mathcal{O}(1$ m/s) variance of the signal of interest.

Thus, using radar observables, it is possible to predict much of the variability in k_r, k_s, and f_s^{PP}. A representative dataset could be used to develop a suitable and globally representative GMF-like algorithm for these unknowns.

The obtained form and corresponding coefficients are anecdotal and not intended to be interpreted as a de facto GMF. Rather, it should be observed that taking into account but a few parameters (incidence angle, the polarization ratio, and a proxy for mean-squared slope) explains much of the observed variability. Such a minimal empirical addition to the existing domain knowledge—which is infused in the analytical form—enables a superior level of prediction.

3) Simplified: This simplified analytical method yields results in line with the idealized DopRIM-GMF implementation, with low variability and good transferability to different regimes and observation geometries. A particular benefit over the previous hybrid approaches is the lessened sensitivity to overfitting, since only one parameter demands estimation. Thus, this simplified approach should better extend to unsampled conditions, which is why it is next applied to the entirely different observations acquired with TanDEM-X.

C. Qualitative Observational Analyses

Of the four methods developed on the California simulation, the simplified method, being the most generalizable, is next applied on two dual-polarized ATI observations (see Fig. 2). The same approximation and constants obtained from the C-band California simulation are expected to transfer well to X-band observations since the wavelength dependence is limited, as observed experimentally in [33]. Indeed, simulations run at the X-band (not shown) yield an X-band estimate of $\tilde{k}_s = 3.60$, while $\tilde{k}_s = 3.97$ results in the lowest mean value for the upper 80-km along-azimuth extent—a region for which a zero-mean TSC may be expected. Following (25), this latter value results in an approximately 20% difference with respect to $\tilde{k}_s = 3.32$ as estimated at the C-band.

1) 2014/08/30: The streaks in the intensity data are oriented along the direction of the surface wind estimated by ECMWF, coming from the West–Northwest at around 7 m/s at the northern part of the image and from the North at around 10 m/s in the southern part (see the left-half of Fig. 2). The drop in the intensity toward the South is consistent with the turn of the wind direction and enhanced by shadowing caused by the cape.

For the Doppler velocities, several aspects need to be noted. First, the Doppler velocity at HH is feature-rich, as highlighted by the features annotated with **A**, **B**, and **C**. These features are absent or muffled in $\tilde{v}_{\mathrm{wD}}$ and Δv^{PP}. A feature-poor $\tilde{v}_{\mathrm{wD}}$ is in line with expectation for a homogeneous offshore wind field. The orientation of **A** is offset with respect to the wind streaks. Both $\tilde{v}_{\mathrm{wD}}$ and Δv^{PP} suggest that this region should experience homogeneous wave Doppler, such that the anomaly is attributed to a minor surface current instead. In Δv^{PP}, one can still identify **B** due to it nearly canceling out with respect

Authorized licensed use limited to: TU Delft Library. Downloaded on December 03,2025 at 16:28:38 UTC from IEEE Xplore. Restrictions apply.

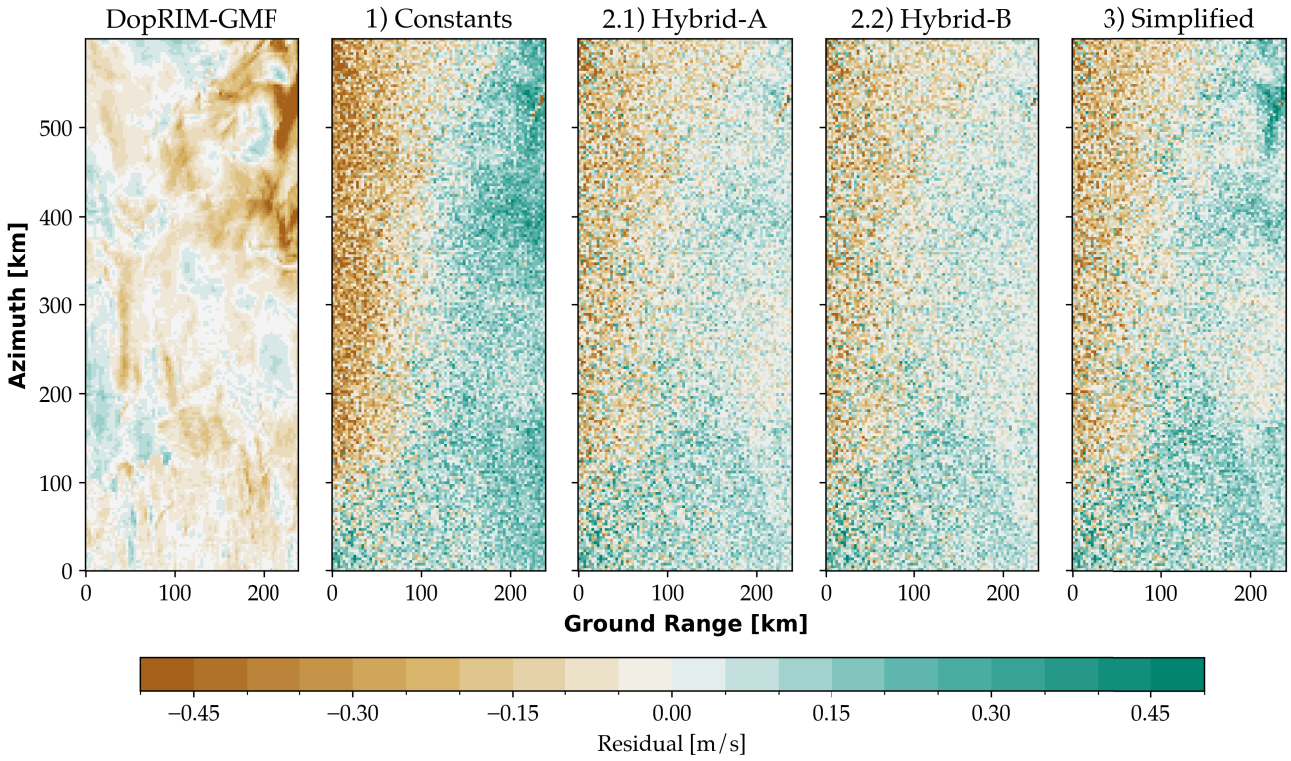

Fig. 4. Spatial residuals of $v_{\mathrm{wD}}^{\mathrm{HH}} - \tilde{v}_{\mathrm{wD}}^{\mathrm{HH}}$ under noisy conditions and coarse-grained to a 3 by 3 km grid. Notably, there are ample geophysical structures present in the residuals for the DopRIM-GMF, while these are absent in methods reliant on polarization diversity. The prevailing along-range trend for these latter four methods is attributed to complications pertaining to the SWB implementation (a several Hz Doppler bias was observed during the SWB development for steeper incident angles when compared to CDOP due to incompatibilities between CMOD and CDOP [unpublished]), which results in an overestimation of Dopplers at steep incidence angles. This bias is known to be a function of the prevailing wind direction, which is indeed observed at the southern turning winds.

to the background. The additional polarization weighting in $\tilde{v}_{\mathrm{wD}}$ compensates this effect such that a relatively homogeneous wave Doppler is maintained without introducing striking artifacts in the estimated surface current. Thus, through the polarimetry-enabled weighting, this component is identified as being of noncurrent origin, which could not be concluded before. Lastly, the dipole structure annotated by **C** is identified as purely current driven: it is entirely absent in $\tilde{v}_{\mathrm{wD}}$, such that it is much amplified in the estimated TSC. Indeed, the location of this dipole coincides with the likely merging of two orthogonal surface currents.

2) 2014/09/10: The low winds coinciding with the later date (see the right-half of Fig. 2) result in a low NRCS, a low signal-to-noise ratio (SNR), and unreliable interpretations. Nonetheless, both this scene and the preceding scene from 2014/08/30 experience similar mean Dopplers and estimated wave Dopplers. Methods reliant on backscatter intensity would struggle to reconcile this behavior.

One region with the elevated NRCS and SNR is annotated by **D**. The observed plume-like structure connects to the mouth of the river Ter. Elevated river discharges were recorded for the Ter on this date [34], suggesting the observed Doppler to be a manifestation of surface currents. Indeed, $\tilde{v}_{\mathrm{wD}}$ does not rise beyond its background value, whereas a much sharper increase is observed in the estimated surface current.

V. Conclusion and Perspectives

This study aims to retrieve the wave-Doppler component of the Doppler budget using polarimetric diversity. Based on a signal model rooted in scattering theory, we exploit the propensity of surface currents and wave Doppler to each impart a characteristic signal onto orthogonal polarizations.

Various approximated forms are presented that provide new and practicable methods for wave-Doppler estimation using dual-polarized observations. And, although shown only using ATI observations, there are no methodological constraints to preclude its application to DCA observations. Though the latter is generally noisier, necessitating more spatial averaging (see [4]).

Of the four presented approximation methods, the first three rely directly on the analytical formulation presented in (11) and try to *fill in the blanks* using empirical information. The fourth method, though also rooted in empiricism, relies on a simplified analytical form as presented in (25). This makes it less cumbersome and well generalizable, as confirmed by the direct applicability to X-band observations.

Quantitative assessments on simulated case studies provide encouraging results: even with gross approximations, wave-Doppler estimation uncertainties—which transfer one-to-one as TSC-estimation uncertainty—are low compared to the dynamic range of the signal of interest, biases are reduced

Authorized licensed use limited to: TU Delft Library. Downloaded on December 03,2025 at 16:28:38 UTC from IEEE Xplore. Restrictions apply.

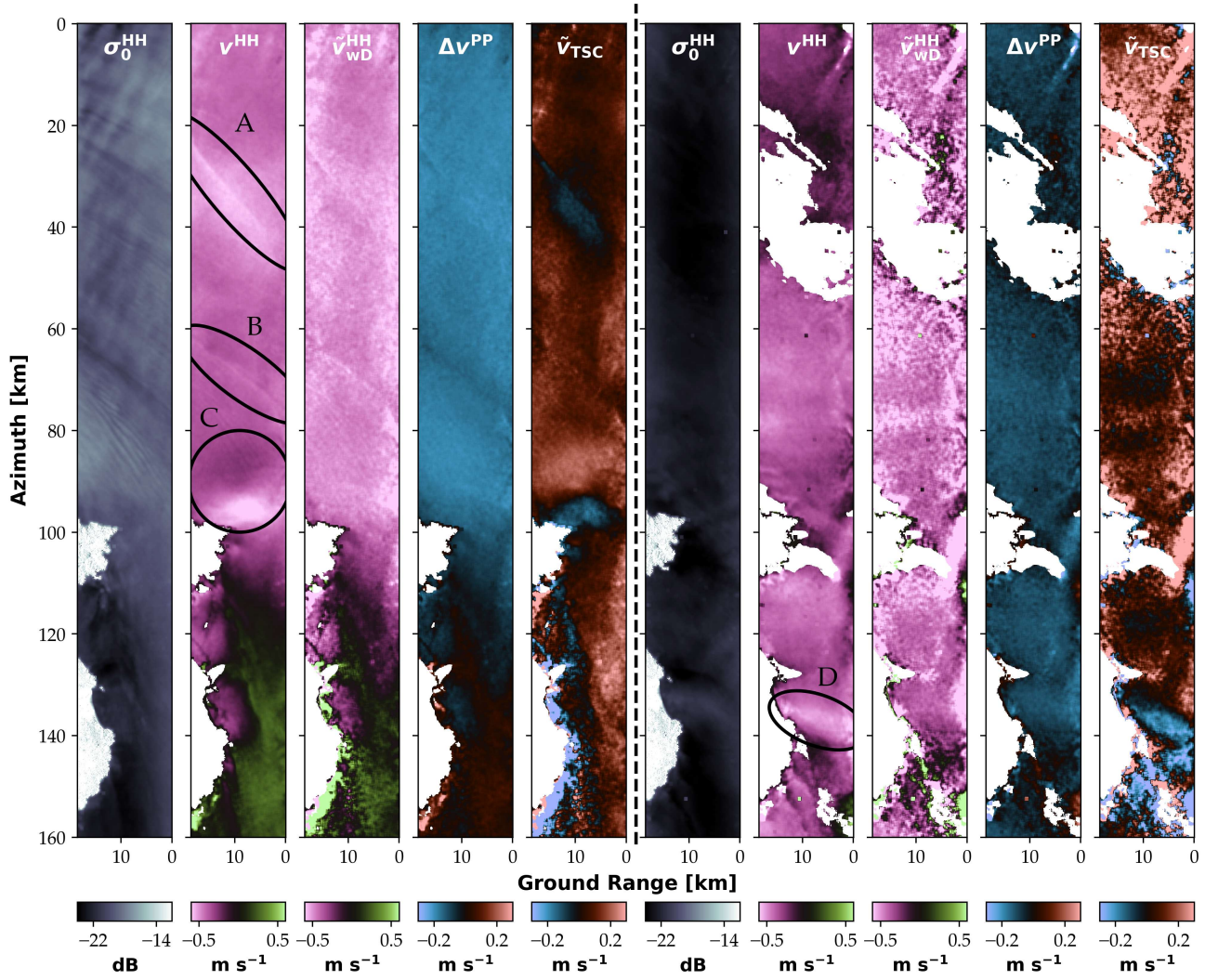

Fig. 5. Observations and inferences over the French Gulf of Lyon in the North, and Spanish Gulf of Roses toward the South on the 2014-08-30 (left-half) and 2014-09-10 (right-half). Bright targets and areas with poor SNRs have been removed. The estimated wave Doppler $\tilde{v}_{wD}$ is obtained using the simplified method with $\tilde{k}_s = 3.32$. The unweighted Doppler difference ($\Delta v^{PP} = v^{VV} - v^{HH}$) is generally feature-poor compared to the individual velocities and intensity data, suggesting that the deviations observed in v^{HH} are of oceanographic origin (except for potential bathymetric effects and wave–wave interactions near the coastline). Particularly noteworthy areas are (a) sharp striation prevalent in the Doppler and not parallel to the main wind-induced streaks present in the NRCS, suggesting an current-related origin, (b) striation coinciding with NRCS gradients with a minor influence on the wave Doppler and TSC, (c) dipole-like structure located at the tip of Cap de Creus where the coastal and weak Gulf of Lion surface current crashes into the stronger Liguro-Provençal-Catalan surface current, and (d) anomalously strong velocity observed at the mouth of the river Ter and coincident with the start of several days of elevated river discharge [34].

with respect to a reference DopRIM-GMF, and performance transfers well between the different ascending and descending geometries.

Furthermore, compared to the residuals of the reference DopRIM-GMF method, there are few discernible geophysical features in the residuals presented in Fig. 4. This is perhaps the main benefit of the proposed methods compared to contemporary GMFs—they enable the extraction of much higher resolution geophysical signals. This fact is not directly evident from the aforementioned summary statistics, which suggests a parity in performance instead. And, based on Fig. 4, much of the residuals in the summary residuals of the proposed methods are in fact related to a known SWB bias permeating into the simulation data as an along-range slope.

Of course, the four proposed methods are sensitive to noise in Doppler in addition to the NRCS, as opposed to the more robust NRCS-reliant GMFs. But it is exactly this sensitivity that enables a more holistic characterization of surface motion. Depending on the scales of interest, one could opt to spatially filter the input Doppler fields to reduce noise. Little spatial resolution has to be traded in this manner as the wave Doppler is generally smooth compared to NRCS modulation (see Fig. 5).

Qualitative assessments on real data yield results in line with expectations. Even for a case with low-wind conditions, the residual Doppler budget—retrieved by removing the estimated wave Doppler from the total Doppler budget—highlights distinct areas with probable surface-current activity.

Authorized licensed use limited to: TU Delft Library. Downloaded on December 03,2025 at 16:28:38 UTC from IEEE Xplore. Restrictions apply.

The results of the quantitative and qualitative analyses illustrate the potential of dual-polarized Doppler and NRCS observations to infer contributions to the Doppler budget for a complex and dynamic set of wind–wave–current conditions. These approximated forms are particularly adept at inferring high-frequency spatial deviations from the mean wave-Doppler field—something contemporary GMFs struggle with by their very nature. There is then an opportunity to combine polarization diversity with existing GMFs in a sort of multiscale model, leveraging the high-frequency resolving power of polarization diversity in combination with the average validity of contemporary GMFs. Indeed, initial testing (not shown) suggests that a union of the two disparate models (SWB-GMF + Hybrid A–B) surpasses any of the previously considered models when using a simple scale separation in the frequency domain.

Results of this study open several opportunities in dual-polarized observations of surface motion. Future studies could do away with the approximations made in this study by investigating alternative retrievals of k_s, k_r, and f_s^{PP}.

Extending from [26], one could also aim for the wave Doppler and TSC retrieval using only polarized NRCS. This necessitates the capability to attach an expected Doppler to an associated scattering mechanism. Such an approach would be particularly useful when neither ATI nor DCA Dopplers are available.

Future missions stand to gain from polarization diversity as well. Due to the angular diversity between the Sentinel-1 transmitter and Harmony's receivers, the received signal contains a dual-polarized component (in addition to cross-polarization) [35]. This is in spite of the fact that the transmitter operates at the conventional co-polarization mode. The SNR for the minor polarization will be significantly reduced (and may even be suppressed by the cross-polarization) when compared to systems interleaving polarized signals. Therefore, significant averaging may be needed to suppress noise, which, as mentioned above, does not necessarily come at a great cost to the spatial resolution of wave-Doppler estimation. And, like in [3], [5], and [6], the aforementioned angular diversity may simultaneously enable a unique vector decomposition of the forces of interest.

APPENDIX A

A. ATI Fundamentals

Here, we recall some of the fundamental concepts and relations. In an ATI system, two radars fly separated by a short separation in the along-track direction, providing a temporal aperture τ_{ATI}, for a pair of observations made under nearly identical geometry. The ATI phase and the Doppler velocity are related by

$$v = \frac{\lambda_0 \cdot \phi_{\mathrm{ATI}}}{4\pi \cdot \tau_{\mathrm{ATI}}} \tag{26}$$

where λ_0 is the wavelength of the radar signal (3.1 cm in this case) and ϕ_{ATI} is the interferometric phase.

In general, especially in a formation flying system like TanDEM-X, there will also be a cross-track baseline component that introduces a sensitivity of the measured interferometric phase to the surface height. Often, this sensitivity is expressed in terms of the so-called height of ambiguity (h_{amb}), that is, the height variation resulting in a 2π phase variation. The cross-track phase component associated with a height variation Δh can be written as

$$\phi_{\mathrm{XTI}} = \frac{2\pi \cdot \Delta h}{h_{\mathrm{amb}}}. \tag{27}$$

This phase can be translated (wrongly) into an equivalent Doppler velocity

$$\Delta v_D = \frac{\lambda_0}{2 \cdot h_{\mathrm{amb}} \cdot \tau_{\mathrm{ATI}}} \cdot \Delta h. \tag{28}$$

The perpendicular baseline was very small, resulting in heights of ambiguity in the order of 400 m or higher. Combined with the temporal lag, this results in a height to velocity conversion factor, as given by (28) of less than 1.5 cm/s/m.

TABLE II
ACQUISITION DATE, ALONG-TRACK TEMPORAL LAG, HEIGHT OF AMBIGUITY, INCIDENT ANGLE, AND ECMWF-REPORTED WIND CONDITIONS FOR THE ACQUISITIONS CONSIDERED

Date	Temporal lag	h_{amb}	Incident angle	ECMWF wind range
2014/08/30	4.6 ms	> 452 m	41°	7 - 10 m s^{-1}
2014/09/10	3.9 ms	> 433 m	41°	0 - 4 m s^{-1}

B. Processing Details

The L1 data were generated by the operational processing chain of the German Aerospace Center (DLR), and interferometrically processed using TAXI (experimental TAnDEM-X Interferometric processor) [36]. For each acquisition, the data was provided in 5 frames, which had to be stitched together.

Following common practices in the along-track interferometry community, the interferometric phase was calibrated using the land areas included in the acquisitions to determine a phase offset, assumed constant for the whole acquisition.

The intensity data and complex interferograms were further multilooked down to a grid spacing of 750 by 750 m^2, providing in the order of 60 000 independent looks. To estimate the normalized radar cross sections, the estimated noise floor was subtracted from the averaged intensities. The acquisitions are about 250-km long with a swath width of approximately 15 km.

It is worth noting that the noise floor changed near the end of the fourth frame toward the end of the acquisition, which has been cut off in the presented figures. We speculate that this was caused by a change in the azimuth-switched block adaptive quantization scheme [37], as the last part of the acquisitions corresponded to areas with a low NRCS.

The temporal lag between the interferometric acquisitions, the height of ambiguity, and the incident angle for the data are reported in Table II. The temporal lags correspond to physical along-track separations between the two satellites ranging from 40 to 70 m, which is around the optimum value in terms of interferometric performance [21].

ACKNOWLEDGMENT

The authors would like to thank the two anonymous reviewers for their helpful additions, as well as Andreas

Authorized licensed use limited to: TU Delft Library. Downloaded on December 03,2025 at 16:28:38 UTC from IEEE Xplore. Restrictions apply.

Theodosiou and Philip Conroy for their assistance toward the custom implementation of the SWB software [38]. Notebooks reproducing the figures of this study are available at https://github.com/owenodriscoll/dualpolati, with the data used therein available at 10.5281/zenodo.17090608. Used software packages include [39] and [40] for visualization, [41], [42], and [43] for general computations, and [44] for the implementation of symbolic regression.

REFERENCES

[1] R. M. Goldstein and H. A. Zebker, "Interferometric radar measurement of ocean surface currents," *Nature*, vol. 328, no. 6132, pp. 707–709, Aug. 1987.

[2] R. Romeiser, H. Breit, M. Eineder, and H. Runge, "Demonstration of current measurements from space by along-track SAR interferometry with SRTM data," in *Proc. IEEE Int. Geosci. Remote Sens. Symp.*, vol. 1, Sep. 2002, pp. 158–160.

[3] J. V. Toporkov, D. Perkovic, G. Farquharson, M. A. Sletten, and S. J. Frasier, "Sea surface velocity vector retrieval using dual-beam interferometry: First demonstration," *IEEE Trans. Geosci. Remote Sens.*, vol. 43, no. 11, pp. 2494–2502, Nov. 2005.

[4] R. Romeiser, H. Runge, S. Suchandt, R. Kahle, C. Rossi, and P. S. Bell, "Quality assessment of surface current fields from TerraSAR-X and TanDEM-X along-track interferometry and Doppler centroid analysis," *IEEE Trans. Geosci. Remote Sens.*, vol. 52, no. 5, pp. 2759–2772, May 2014.

[5] S. J. Frasier and A. J. Camps, "Dual-beam interferometry for ocean surface current vector mapping," *IEEE Trans. Geosci. Remote Sens.*, vol. 39, no. 2, pp. 401–414, Feb. 2001.

[6] N. Caldarella et al., "Retrieval of wind and total surface current vectors using experimental bidirectional along-track interferometric TanDEM-X data," *IEEE Trans. Geosci. Remote Sens.*, vol. 60, 2022, Art. no. 5223412.

[7] B. Chapron, F. Collard, and F. Ardhuin, "Direct measurements of ocean surface velocity from space: Interpretation and validation," *J. Geophys. Res., Oceans*, vol. 110, no. C7, pp. 1–17, Jul. 2005.

[8] M. W. Hansen et al., "Simulation of radar backscatter and Doppler shifts of wave–current interaction in the presence of strong tidal current," *Remote Sens. Environ.*, vol. 120, pp. 113–122, May 2012.

[9] D. R. Thompson and J. R. Jensen, "Synthetic aperture radar interferometry applied to ship-generated internal waves in the 1989 loch linnhe experiment," *J. Geophys. Res., Oceans*, vol. 98, no. C6, pp. 10259–10269, Jun. 1993.

[10] L. Cavaleri, B. Fox-Kemper, and M. Hemer, "Wind waves in the coupled climate system," *Bull. Amer. Meteorological Soc.*, vol. 93, no. 11, pp. 1651–1661, Nov. 2012.

[11] S. Chen, F. Qiao, C. J. Huang, and B. Zhao, "Deviation of wind stress from wind direction under low wind conditions," *J. Geophys. Res., Oceans*, vol. 123, no. 12, pp. 9357–9368, Dec. 2018.

[12] C. J. Huang and F. Qiao, "Wave-turbulence interaction and its induced mixing in the upper ocean," *J. Geophys. Res., Oceans*, vol. 115, no. C4, pp. 1–12, Apr. 2010.

[13] A. A. Mouche et al., "On the use of Doppler shift for sea surface wind retrieval from SAR," *IEEE Trans. Geosci. Remote Sens.*, vol. 50, no. 7, pp. 2901–2909, Jul. 2012.

[14] F. Saïd and H. Johnsen, "Ocean surface wind retrieval from dual-polarized SAR data using the polarization residual Doppler frequency," *IEEE Trans. Geosci. Remote Sens.*, vol. 52, no. 7, pp. 3980–3990, Jul. 2014.

[15] V. Zamparelli, F. De Santi, G. De Carolis, and G. Fornaro, "SAR based sea surface complex wind fields estimation: An analysis over the northern Adriatic sea," *Remote Sens.*, vol. 15, no. 8, p. 2074, Apr. 2023.

[16] X.-M. Li and S. Lehner, "Algorithm for sea surface wind retrieval from TerraSAR-X and TanDEM-X data," *IEEE Trans. Geosci. Remote Sens.*, vol. 52, no. 5, pp. 2928–2939, May 2014.

[17] Y. Y. Yurovsky, V. N. Kudryavtsev, S. A. Grodsky, and B. Chapron, "Sea surface Ka-band Doppler measurements: Analysis and model development," *Remote Sens.*, vol. 11, no. 7, p. 839, Apr. 2019.

[18] V. Kudryavtsev, D. Akimov, J. Johannessen, and B. Chapron, "On radar imaging of current features: 1. Model and comparison with observations," *J. Geophys. Res., Oceans*, vol. 110, no. C7, pp. 1–27, Jul. 2005.

[19] A. Moiseev, H. Johnsen, J. A. Johannessen, F. Collard, and G. Guitton, "On removal of sea state contribution to Sentinel-1 Doppler shift for retrieving reliable ocean surface current," *J. Geophys. Res., Oceans*, vol. 125, no. 9, p. 2020, Sep. 2020.

[20] A. Moiseev, J. A. Johannessen, and H. Johnsen, "Towards retrieving reliable ocean surface currents in the coastal zone from the Sentinel-1 Doppler shift observations," *J. Geophys. Res., Oceans*, vol. 127, no. 5, p. 2021, May 2022.

[21] S. Wollstadt, P. Lopez-Dekker, F. De Zan, and M. Younis, "Design principles and considerations for spaceborne ATI SAR-based observations of ocean surface velocity vectors," *IEEE Trans. Geosci. Remote Sens.*, vol. 55, no. 8, pp. 4500–4519, Aug. 2017.

[22] C. Gommenginger et al., "SEASTAR: A mission to study ocean submesoscale dynamics and small-scale atmosphere-ocean processes in coastal, shelf and polar seas," *Frontiers Mar. Sci.*, vol. 6, p. 457, Mar. 2019.

[23] R. K. Raney, "Hybrid-polarity SAR architecture," *IEEE Trans. Geosci. Remote Sens.*, vol. 45, no. 11, pp. 3397–3404, Nov. 2007.

[24] P. López-Dekker, H. Rott, P. Prats-Iraola, B. Chapron, K. Scipal, and E. D. Witte, "Harmony: An Earth explorer 10 mission candidate to observe land, ice, and ocean surface dynamics," in *Proc. IEEE Int. Geosci. Remote Sens. Symp. (IGARSS)*, Jul. 2019, pp. 8381–8384.

[25] G. Krieger et al., "TanDEM-X: A satellite formation for high-resolution SAR interferometry," *IEEE Trans. Geosci. Remote Sens.*, vol. 45, no. 11, pp. 3317–3341, Nov. 2007.

[26] V. N. Kudryavtsev, B. Chapron, A. G. Myasoedov, F. Collard, and J. A. Johannessen, "On dual co-polarized SAR measurements of the ocean surface," *IEEE Geosci. Remote Sens. Lett.*, vol. 10, no. 4, pp. 761–765, Jul. 2013.

[27] V. Kudryavtsev, I. Kozlov, B. Chapron, and J. A. Johannessen, "Quad-polarization SAR features of ocean currents," *J. Geophys. Res., Oceans*, vol. 119, no. 9, pp. 6046–6065, Sep. 2014.

[28] V. Kudryavtsev, D. Hauser, G. Caudal, and B. Chapron, "A semiempirical model of the normalized radar cross-section of the sea surface 1. Background model," *J. Geophys. Res., Oceans*, vol. 108, no. C3, pp. 1–24, Mar. 2003.

[29] J. A. Johannessen et al., "Direct ocean surface velocity measurements from space: Improved quantitative interpretation of ENVISAT ASAR observations," *Geophys. Res. Lett.*, vol. 35, no. 22, pp. 1–6, 2008.

[30] V. Kudryavtsev, S. Fan, B. Zhang, B. Chapron, J. A. Johannessen, and A. Moiseev, "On the use of dual co-polarized radar data to derive a sea surface Doppler model—Part 1: Approach," *IEEE Trans. Geosci. Remote Sens.*, vol. 61, 2023, Art. no. 4201013.

[31] N. Booij, L. Holthuijsen, and R. Ris, "The 'swan' wave model for shallow water," in *Coastal Engineering 1996*. Reston, VA, USA: ASCE, 1996, pp. 668–676.

[32] T. Elfouhaily, B. Chapron, K. Katsaros, and D. Vandemark, "A unified directional spectrum for long and short wind-driven waves," *J. Geophys. Res., Oceans*, vol. 102, no. C7, pp. 15781–15796, Jul. 1997.

[33] A. C. H. Martin, C. Gommenginger, J. Marquez, S. Doody, V. Navarro, and C. Buck, "Wind-wave-induced velocity in ATI SAR ocean surface currents: First experimental evidence from an airborne campaign," *J. Geophys. Res., Oceans*, vol. 121, no. 3, pp. 1640–1653, Mar. 2016.

[34] A. C. de l'Aigua. (2025). *River Volume Flow*. Accessed: May 8, 2024. [Online]. Available: https://aplicacions.aca.gencat.cat/sdim21/

[35] L. Iannini, D. Comite, N. Pierdicca, and P. Lopez-Dekker, "Rough-surface polarimetry in companion SAR missions," *IEEE Trans. Geosci. Remote Sens.*, vol. 60, 2022, Art. no. 2004915.

[36] P. Prats et al., "Taxi: A versatile processing chain for experimental TanDEM-X product evaluation," in *Proc. IEEE Int. Geosci. Remote Sens. Symp.*, Jul. 2010, pp. 4059–4062.

[37] M. Martone, B. Bräutigam, and G. Krieger, "Azimuth-switched quantization for SAR systems and performance analysis on TanDEM-X data," *IEEE Geosci. Remote Sens. Lett.*, vol. 11, no. 1, pp. 181–185, Jan. 2014.

[38] P. López-Dekker, M. Kleinherenbrink, A. Theodosiou, P. Conroy, and L. Gaultier, "The stereoid tools for the harmony mission," Delft Univ. Technol., Delft, The Netherlands, Tech. Rep., 2024. [Online]. Available: https://pypi.org/project/stereoid/0.4/

[39] F. Crameri, "Scientific colour maps," Tech. Rep., 2023, doi: 10.5281/zenodo.8035877.

[40] M. Waskom, "Seaborn: Statistical data visualization," *J. Open Source Softw.*, vol. 6, no. 60, p. 3021, Apr. 2021, doi: 10.21105/joss.03021.

[41] S. Hoyer and J. Hamman, "Xarray: N-D labeled arrays and datasets in Python," *J. Open Res. Softw.*, vol. 5, no. 1, p. 10, Apr. 2017, doi: 10.5334/jors.148.

Authorized licensed use limited to: TU Delft Library. Downloaded on December 03,2025 at 16:28:38 UTC from IEEE Xplore. Restrictions apply.

[42] C. R. Harris et al., "Array programming with NumPy," *Nature*, vol. 585, no. 7825, pp. 357–362, 2020.
[43] W. McKinney, "Data structures for statistical computing in Python," in *Proc. Python Sci. Conf.*, Apr. 2010, pp. 56–61.
[44] M. Cranmer, "Interpretable machine learning for science with PySR and SymbolicRegression.Jl," 2023, *arXiv:2305.01582*.

Owen O'Driscoll received the master's degree (cum laude) from the Civil Engineering Faculty, Delft University of Technology, Delft, The Netherlands, in 2021, where he is currently pursuing the Ph.D. degree in radar oceanography with the Geoscience and Remote Sensing Department.

From 2022 to 2023, he was with the Oceanography from Space Laboratory, Ifremer, Plouzané, France, to study air–sea interactions with spaceborne radars.

Paco López-Dekker (Senior Member, IEEE) was born in Nijmegen, The Netherlands, in 1972. He received the Ingeniero degree in telecommunication engineering from Universitat Politécnica de Catalunya (UPC), Barcelona, Spain, in 1997, the M.S. degree in electrical and computer engineering from the University of California at Irvine, Irvine, CA, USA, in 1998, under the Balsells Fellowship, and the Ph.D. degree in clear-air imaging radar systems to study the atmospheric boundary layer from the University of Massachusetts, Amherst, MA, USA, in 2003.

In 2003, he joined Starlab Barcelona, Barcelona, where he worked on the development of Global Navigation Satellite Systems-Reflectometry (GNSS-R) sensors and techniques. From 2004 to 2006, he was a Visiting Professor with the Department of Telecommunications and Systems Engineering, Universitat Autónoma de Barcelona, Bellaterra, Spain. In March 2006, he was awarded a Ramon y Cajal Grant to conduct pioneering research on bistatic synthetic aperture radar (SAR) at the Remote Sensing Laboratory, UPC. From November 2009 to August 2016, he led the SAR Missions Group, Microwaves and Radar Institute, German Aerospace Center, Weßling, Germany. Since September 2016, he has been an Associate Professor with the Geoscience and Remote Sensing Department, Faculty of Civil Engineering and Geosciences, Delft University of Technology, Delft, The Netherlands. He has been deeply involved in the development of several radar missions and mission proposals and is the Lead Investigator of the Harmony European Space Agency (ESA) Earth Explorer 10 Mission. He has co-authored over 50 peer-reviewed journal articles and more than 125 conference contributions in a broad range of topics related to radar remote sensing.

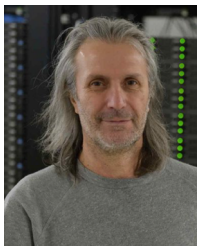

Bertrand Chapron received the Ph.D. degree in fluid mechanics from Aix-Marseille University, Marseille, France, in 1988.

He is currently a Senior Research Scientist with the Laboratoire d'Océanographie Physique Spatiale, Institut Francais de Recherche pour l'Exploitation de la Mer, Plouzané, France. He has been a Co-Investigator or a Principal Investigator in several ESA (ENVISAT RA2, ASAR, and SMOS), NASA, and CNES (TOPEX and JASON) projects. He contributed to the development of several algorithms for geophysical parameter retrieval from altimeters, radiometers, or SAR. He is co-responsible for the ENVISAT ASAR-Wave Mode algorithms and scientific preparation for the ENVISAT and S1 wind, wave, and current retrieval. Recently, he collaborated in studies that demonstrated the high potential of radiometers for wind retrieval in extreme conditions and the possibility of doing a directional ocean wave spectrum from Sentinel-2. He has authored over 80 publications in refereed journals in applied mathematics, physical oceanography (upper ocean dynamics), and electromagnetic wave theory and its application to ocean surface remote sensing.

Authorized licensed use limited to: TU Delft Library. Downloaded on December 03,2025 at 16:28:38 UTC from IEEE Xplore. Restrictions apply.